3D variable-density SPARKLING trajectories for high-resolution T2*-weighted Magnetic Resonance imaging

Carole Lazarus, Pierre Weiss, Loubna El Gueddari, Franck Mauconduit, Aurélien Massire, Mathile Ripart, Alexandre Vignaud, Philippe Ciuciu

3D variable-density SPARKLING trajectories for high-resolution T2*-weighted Magnetic Resonance imaging

Carole Lazarus[1,2,3], Pierre Weiss[4,5,6], Loubna El Gueddari[1,2,3], Franck Mauconduit[7], Aurélien Massire[1], Mathile Ripart[1,2], Alexandre Vignaud[1,2], and Philippe Ciuciu[1,2,3]

[1]CEA, CNRS, BAOBAB, NeuroSpin, 91191 Gif-sur-Yvette cedex, France
[2]Université Paris-Saclay, France
[3]INRIA, Parietal, 91120 Palaiseau, France
[4]ITAV USR3505 CNRS, 31000 Toulouse, France
[5]IMT UMR 5219 CNRS, 31400 Toulouse, France
[6]Université de Toulouse, France
[7]Siemens Healthineers, 93210 Saint-Denis, France

***Abstract*—We have recently proposed a new optimization algorithm called SPARKLING (Spreading Projection Algorithm for Rapid K-space sampLING) to design efficient Compressive Sampling patterns for Magnetic Resonance Imaging. This method has a few advantages over conventional non-Cartesian trajectories such as radial lines or spirals: i) it allows to sample the k-space along any arbitrary density while the other two are restricted to radial densities and ii) it optimizes the gradient waveforms for a given readout time. Here, we introduce an extension of the SPARKLING method for 3D imaging by considering both stacks-of-SPARKLING and fully 3D SPARKLING trajectories. Our method allowed to achieve an isotropic resolution of 600 μm in just 45 seconds for T2*-weighted ex vivo brain imaging at 7 Tesla over a field-of-view of $200 \times 200 \times 140$ mm^3. Preliminary human brain data shows that a stack-of-SPARKLING is less subject to off-resonance artifacts than a stack-of-spirals.**

***Index Terms*—3D MRI, optimization, non-Cartesian, compressed sensing, acceleration, SWI.**

I. Introduction

To reduce scan time in MRI, sampling along non-Cartesian trajectories may prove to be advantageous. An efficient use of the MR gradient hardware can indeed enable rapid coverage of the k-space. When combined with Compressed Sensing, the use of undersampled non-Cartesian trajectories can allow further reduction in the acquisition time [1]. In this context, it was shown that k-space trajectories should be distributed along a variable density sampling for best performance [2]–[4].

Three-dimensional (3D) compressed acquisitions are usually performed with 3D radial trajectories [5] or a Poisson-disk strategy [6]. The former observes a fully 3D variable density while the latter performs a 2D Poisson-disk variable density orthogonally to the readout lines. Let us mention a few other fully 3D sampling strategies based on analytical expression such as 3D cones [7], twisted projections (TPI) [8], hybrid radial-cones [10] and more [9]. However, these methods are restricted to a certain type of sampling densities (e.g. radial or cylindrical), which may limit their efficiency. A few works attempted to use optimization principles to design 3D trajectories [11]–[13], but did not include clear sampling criteria.

Recently, we have introduced a new optimization-driven method named SPARKLING (Spreading Projection Algorithm for Rapid K-space samplING) [14]–[16]. This algorithm inspired from stippling techniques automatically generates optimized non-Cartesian sampling patterns compatible with MR hardware constraints on maximum gradient amplitude and slew rate. These sampling curves are designed to comply with key criteria for optimal sampling: a controlled distribution of samples (e.g., a variable density) and a locally uniform k-space coverage. The SPARKLING strategy was used for 2D T_2^* high-resolution in vivo brain imaging and was shown to yield higher image quality compared to conventional non-Cartesian geometrical patterns such as radial or spiral trajectories, while allowing to reduce scan time by a factor up to 20 compared to standard Cartesian scans [16]. The proposed method may hence propose a good trade-off between sampling efficiency and robustness to artifacts.

In this paper, we explore how the principles of the SPARKLING method can be extended to design 3D trajectories, expecting to benefit from a higher signal-to-noise ratio (SNR). We begin by exploring the use of stacks of 2D SPARKLING trajectories (in the same way as stack-of-stars [17], [18], stack-of-spirals [7], [19] or stack of EPI [20]). Then, we turn to fully 3D SPARKLING trajectories, which have the potential to respect a truly 3D variable density necessary for an optimal use of Compressed Sensing in 3D [21], [22].

We used the SPARKLING strategy to accelerate 3D prospective high-resolution T_2^*-weighted MR acquisitions at 7 Tesla. For the sake of contrast, the echo time of

T_2^*- or susceptibility-weighted imaging (SWI) at 7 Tesla is often high [23]–[25]. This makes standard Cartesian Gradient Recalled Echo (GRE) sequence highly inefficient for this type of acquisition, and leaves room for acceleration with longer-readout sampling trajectories which use the gradients more efficiently. Thus, we chose to work with long readout durations of 15 to 20 ms, which allow to cover more of k-space in each shot, thereby reducing the number of shots and speeding up the acquisition, compared to standard sampling. As highlighted in [16], the regime of longer readouts is also a situation where the SPARKLING algorithm is able to significantly improve the initial input trajectory, thus allowing to accelerate the acquisition even more. We compared our method against several standard 3D sampling strategies including Cartesian scans for reference images. For the ex vivo study, acquisitions were performed with two non-Cartesian trajectories which allow to perform variable density sampling in the context of Compressed Sensing: 3D radial [5] and a Poisson-disk approach [6]. Furthermore, we show preliminary results of 3D T_2^*-weighted in vivo acquisitions comparing a stack-of-SPARKLING to a stack-of-spirals.

II. Theory: Optimization-driven design of sampling patterns in MRI

A. 2D k-space trajectories

A k-space trajectory is usually composed of several segments $\mathbf{k}(t) = (k_x(t), k_y(t))$, also referred to as shots, which are controlled by magnetic field gradients $\mathbf{G}(t) = (G_x(t), G_y(t))$ as follows:

$$\mathbf{k}(t) = \frac{\gamma}{2\pi} \int_0^t \mathbf{G}(\tau) d\tau \,, \tag{1}$$

where γ denotes the gyro-magnetic ratio. Hardware constraints on the maximum gradient amplitude (G_{max}) and slew rate (S_{max}) induce limitations in trajectory speed and acceleration. These limits can be expressed as inequality range constraints on each of the time points of the discrete waveform $\mathbf{k} = (\mathbf{k}[i])_{1 \le i \le p}$ where $\mathbf{k}[i] = (k_x[i], k_y[i]), \forall 1 \le i \le p$ and p is the number of gradient time-steps. Typically, rotation invariant speed and acceleration constraints can be expressed as follows:[1]

$$\|\dot{\mathbf{k}}\|_{2,\infty} < \frac{\gamma}{2\pi} G_{max} \quad \text{(2a)} \qquad \|\ddot{\mathbf{k}}\|_{2,\infty} < \frac{\gamma}{2\pi} S_{max} \quad \text{(2b)}$$

where $\|\mathbf{c}\|_{2,\infty} = \sup_{1 \le i \le p} \left(|\mathbf{c}_x[i]|^2 + |\mathbf{c}_y[i]|^2 \right)^{1/2}$ and

$$\begin{cases} \dot{\mathbf{k}}[i] &= \frac{\mathbf{k}[i] - \mathbf{k}[i-1]}{dt}, \\ \ddot{\mathbf{k}}[i] &= \frac{\mathbf{k}[i+1] - 2\mathbf{k}[i] + \mathbf{k}[i-1]}{dt^2} \end{cases} \tag{3}$$

Here dt is the gradient raster time and in practice it may be different from the dwell time Δt.

[1] In [26], we have also dealt with the case of rotation variant constraints where the ℓ_∞-norm replaces the mixed $\ell_{2,\infty}$-norm here.

Following [16], we let $\mathcal{Q}_p$ denote the set of p-dimensional k-space discrete curves $\mathbf{k}$ respecting the aforementioned constraints (2). Note that $\mathcal{Q}_p$ can be completed to account for any affine constraint such as the specification of $\mathbf{k}$ at the echo-time (TE): $\mathbf{k}[TE] = 0$. In the context of multi-shot acquisitions, these constraints apply to every shot independently. In the next section, we briefly remind the minimization problem we solve in the SPARKLING algorithm framework [15], [16] to point out the challenges raised in 3D imaging afterwards.

B. The SPARKLING algorithm

Our objective is to minimize a ℓ_2 distance between a target density $\rho : \mathbb{R}^3 \to \mathbb{R}$ and a sampling trajectory $\mathbf{k}$ under the aforementioned constraints (2):

$$\min_{\mathbf{k} \in \mathcal{Q}_p} dist(\rho, \nu(\mathbf{k})) = \min_{\mathbf{k} \in \mathcal{Q}_p} \frac{1}{2} \|h \star (\nu(\mathbf{k}) - \rho)\|_2^2 \tag{4}$$

where h is a continuous interpolation kernel, symbol $\star$ denotes the convolution operator, $\nu(\mathbf{k})$ is the discrete measure supported by the curve $\mathbf{k}$ (see [14] for the definition of ν and more details). The distance in Eq. (4) can be conveniently rewritten by expanding the ℓ_2-norm into:

$$\min_{\mathbf{k} \in \mathcal{Q}_p} \underbrace{\frac{1}{p} \sum_{i=1}^{p} \int_\Omega H(x - \mathbf{k}[i]) \rho(x) \, dx}_{F_{\mathrm{a}}(\mathbf{k})} - \underbrace{\frac{1}{2p^2} \sum_{1 \le i,j \le p} H(\mathbf{k}[i] - \mathbf{k}[j])}_{F_{\mathrm{r}}(\mathbf{k})} \tag{5}$$

where Ω denotes the sampling domain, and the Fourier transform $\hat{H}$ of H is equal to $|\hat{h}|^2$. In our experiments, we selected the Euclidean distance $H(x) = \|x\|_2$ [15], [27]. Problem (5) can be interpreted as the minimization of a potential energy $F = F_{\mathrm{a}} - F_{\mathrm{r}}$ containing an attractive term F_{a} (bringing together samples according to the target density ρ) and a repulsive term F_r (avoiding the formation of gaps and clusters of samples). Although the cost function is non-convex, F_a and F_r are differentiable, so the calculation of their gradient (∇F_a and ∇F_r, respectively) is feasible, and the global cost function can be *locally* minimized by a projected gradient descent of the type $\mathbf{k}_{t+1} = \Pi_{\mathcal{Q}_p} (\mathbf{k}_t - \beta_t \nabla F(\mathbf{k}_t))$ where $\nabla F = \nabla F_a - \nabla F_r$. This algorithm alternates between a non-convex distance minimization part and a projection onto the convex MR constraints $\mathcal{Q}_p$. We refer to [28] for more details on the computation of the gradient ∇F and to [26] for details about the projection on $\mathcal{Q}_p$.

C. Stack-of-SPARKLING

A first strategy to perform 3D imaging with the SPARKLING method is to use 2D SPARKLING trajectories and stack them along the partition direction which is here the z-axis. This approach is illustrated in Fig. 1**a** for a stack of 10 identical SPARKLING trajectories, which will be referred to as *regular stack-of-SPARKLING* or *regular SoSPARKLING*. To respect the Nyquist criterion

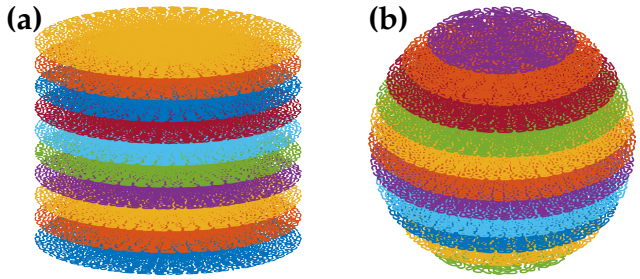

Fig. 1. Two versions of stack-of-SPARKLING trajectories. (**a**): a stack of 10 identical SPARKLING trajectories filling a cylinder. (**b**): a stack of 11 variable SPARKLING trajectories filling a 3D ball. (Colors are for visualization purposes).

along the partition direction, the N_z SPARKLING planes should be spaced by a FOV_z^{-1}-distance until reaching the desired maximum spatial frequency. To increase the incorehence in the z-axis, these planes were rotated by the golden angle. In the situation of a regular SoSPARKLING, no variable density is performed along the partition direction.

To additionally subsample the partition direction and obtain a fully 3D variable density, the target density may be changed according to the plane's altitude k_z. Given a 3D density $\rho \in \mathbb{R}^{N\times N\times N_z}$, a 2D SPARKLING trajectory at altitude k_z will be generated using the density $\rho_{2D}(k_z) = \frac{\rho(:,:,k_z)}{\int \rho(:,:,k_z)}$. In addition, once the number of shots in the central stack $n(0)$ is chosen, the mass of each plane can be adapted to the plane density by reducing the number of shots per altitude, as k_z increases:

$$n(k_z) = n(0)\frac{\int \rho(:,:,k_z)}{\int \rho(:,:,0)}, \tag{6}$$

where $n(k_z)$ is the number of shots in the plane of altitude k_z. Fig. 1**b** shows such a stack for an isotropic density (defined on a 3D ball) for 10 SPARKLING trajectories. This design will be referred to as *3D-variable-density stack-of-SPARKLING* or *3D-VD SoSPARKLING*. Further acceleration may be reached by subsampling the number of planes and using parallel imaging along this direction.

D. Fully 3D SPARKLING

To perform a fully 3D sampling of the k-space, it is also possible to extend the SPARKLING algorithm presented in [15] to three dimensions. Such segmented sampling scheme is composed of non-Cartesian curves spanning all 3 k-space directions, filling a ball of radius k_{max}, where k_{max} is the maximum radial extent in the 3D k-space.

1) Algorithmic extension: The SPARKLING algorithm's bottleneck lies in the calculation of the gradient of the repulsive term F_r between the samples in Eq. (5), where there is a summation over all the samples. In 3D, this summation was calculated directly using a two-level nested loop, which gives a complexity of $O(p^2)$, where p is the number of particles in $\mathbf{k}$. For high resolution imaging, we need of the order of $p = 10^7$ particles, making this method irrelevant. The 'brute-force' method could be accelerated using 3D techniques used for the simulation of particles (e.g. NFFT or fast multipole methods), but would require complex numerical libraries. In this work, since our objective is to target *radial densities*, which ensure rotation invariant reconstruction results, we propose an alternative technique described below.

2) Using a regular sphere tessellation to accelerate the process: The idea is to generate each shot independently from the others, by truncating the target density into n_s volumetric sectors filling the considered k-space, where n_s is the desired total number of shots. To further accelerate the process, we can reduce the number of SPARKLING-processed shots by using a semi-regular partition of the sphere. We used an equal-area tessellation which divides the sphere into regions of equal area [29], as is displayed in Fig. 2**a** for $n_s = 100$. The property of equal area is important insofar as it ensures that all 3D sectors have equal mass in the case of a radial density. Furthermore, for a constant elevation angle (highlighted in blue on Fig. 2**a**-**b**), all tiles are exactly identical and the associated trajectory can be obtained from another one using a simple rotation. Hence, only a small fraction of the desired total number of shots needs to be generated, namely one per latitude. This leads to a reduction in computation time by a factor 20 to 30. Using this strategy, the typical computational time to generate 1000 shots for a matrix size of $N = 256$ is about 20 minutes on a Intel Xeon(R) CPU at 2.20 GHz with 40 cores.

In the case of center-out shots, a 3D sector is created by connecting the four summits of a spherical tile to the origin of the k-space. If symmetric shots for which the echo time TE is at the middle of the segment, are desired, the latter sector constitutes one half of total symmetric sector and the other half is obtained by rotating the latter about the origin, as displayed in Fig. 2**b**. To avoid discontinuity between the two halves, the sector is slightly thickened near the origin. For example, with this strategy, only 7 symmetric shots need to be produced by the SPARKLING algorithm for $n_s = 100$. Fig. 2**b** shows one SPARKLING shot, corresponding to the highlighted sector for a radially decaying density and for a matrix size of $128 \times 128 \times 128$, $k_{max} = 320\,\text{m}^{-1}$, $G_{max} = 40$ mT/m and $S_{max} = 200$ T/m/s. This shot is then rotated to fill the regions of equal elevation angle, as depicted in Fig. 2**c**. The process is repeated for all latitudes, generating the fully 3D SPARKLING trajectory shown in Fig. 2**d**.

E. Selection of the target density

In view of the long computation time required for reconstructing 3D MR images (i.e. several hours), the target density was retrospectively selected among a set of 6 radially decaying densities. We consider here a radial

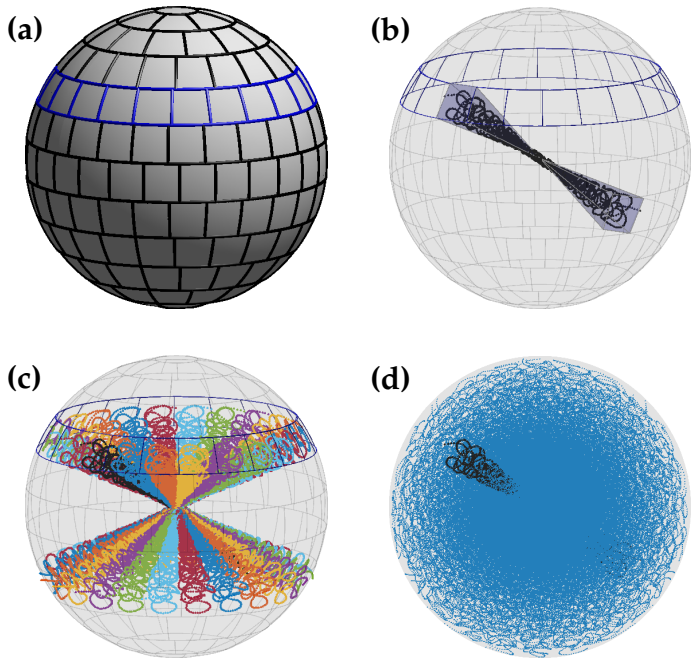

Fig. 2. 3D SPARKLING process. (**a**): Partition of the sphere into 100 regions of equal area. Regions along a constant elevation angle were highlighted in blue: they are identical up to a rotation. (**b**): One 3D density sector containing a SPARKLING shot. (**c**): The SPARKLING shot is then rotated along the considered latitude. (**d**): the whole fully 3D SPARKLING trajectory. An individual segment is highlighted in black. Parameters are: $N = 128$, $k_{max} = 320\,\mathrm{m}^{-1}$, 100 symmetric shots and 7 shots to generate (6 latitudes + 1 conic cap).

isotropic density of the form $\rho : \mathbf{k} \mapsto \frac{1}{|\mathbf{k}|^d}$, which decays as an inverse polynomial. Radial densities present the advantage of yielding results invariant to translation and rotation of the object to be imaged. The singularity at the origin is truncated by the method introduced in [16] allowing to create a circular plateau at Shannon's rate at the origin. Two parameters of the density were varied here: the decay rate $d \in \{2, 3\}$ and the plateau threshold $\tau \in \{0.5, 0.75, 1\}$. Fig. 3 shows the 6 tested densities for $N = 320$. To rank the different densities,

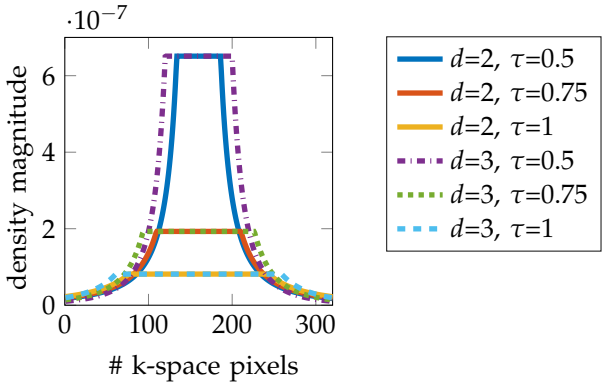

Fig. 3. 1D view of the 6 tested radial densities for $N = 320$. The x-axis is the pixel number while the y-axis is the amplitude of the density.

evenly spaced samples were drawn along each density by using Lloyd's algorithm, also known as Voronoi iteration [30]. Lloyd's method allows to quickly produce a distribution of points with blue noise characteristics, i.e. to produce a locally uniform coverage. The initial positions of the p samples were determined with an i.i.d. drawing along the considered density. Then, Lloyd's algorithm was applied using 10 cycles. Once the 3D samples are produced for $p = 10^6$ and all densities, the corresponding retrospectively generated Fourier data of a 3D baboon brain image are reconstructed using nonlinear 3D reconstructions (details about image reconstruction are provided in Section IV). The density which gives the best image quality both visually and in terms of pSNR is selected and will be used as a 3D target density for the SPARKLING trajectories. For instance, in the case of $N = 320$, we selected the density with $d = 3$ and $\tau = 0.75$.

III. Materials and Methods

A. Protocols

3D prospective acquisitions were performed on a 7 Tesla MR scanner (Siemens Healthineers, Erlangen, Germany) with a 1Tx/32Rx head coil (Nova Medical, Wilmington, MA, USA). The maximum gradient amplitude and slew rate for this system were 40 mT/m and 200 T/m/s, respectively. A 3D Gradient Recalled Echo (GRE) sequence was used. Following standard T2*-weighted and susceptibility-weighted protocols at 7 Tesla [23]–[25], we used an echo time TE=20 ms, a repetition time TR=40 ms and a flip angle FA=15°. We took advantage of these parameters to acquire during a readout window of 15.36 ms with a receiver bandwith of 200 kHz. These parameters were kept constant for all ex vivo experiements conducted on a baboon brain conserved in a fluorinert solution. All animal studies were conducted in accordance with the European convention for animal care and the NIHs Guide for the Care and Use of Laboratory Animals. Moreover, we performed a set of in vivo aquisitions on a healthy volunteer, which were approved by a national ethics committee (CPP 100048). The volunteer signed a written informed consent form. For in vivo experiements, a TR of 37 ms was used and a readout window of 20 ms with a receiver bandwith of 200 kHz.

B. Sampling trajectories

Table I summarizes the studied protocols and the different acceleration setups. The acceleration factor AF is calculated as a function of the fully-sampled Cartesian scan; it is given as the ratio of the number of lines in the reference scan over the number of shots in the accelerated scan (see its formula in Table I).

First, the three proposed SPARKLING trajectories were compared for an isotropic resolution of 0.6 mm: regular SoSPARKLING, 3D-VD SoSPARKLING and fully 3D SPARKLING. As reference, we also performed a standard Cartesian iPAT acquisition with GRAPPA reconstruction available on the scanner (Siemens product

TABLE I
IMAGING AND SAMPLING PARAMETERS USED IN EX VIVO (DARK GREY) AND IN VIVO (LIGHT GRAY) ACQUISITIONS.

FOV (mm^3)	Matrix size	Resolution (mm)	Number of shots n_s	Total scan time (TA)	AF $= \frac{N \times N_z}{n_s}$
$200 \times 200 \times 140$	$320 \times 320 \times 224$	$0.6 \times 0.6 \times 0.6$	4010	2 min 40 s	18
			2050	1 min 22 s	35
			1140	45 s	63
$200 \times 200 \times 140$	$640 \times 640 \times 96$	$0.3 \times 0.3 \times 1.5$	4085	2 min 43 s	15
			2090	1 min 24 s	30
$230 \times 230 \times 124$	$384 \times 384 \times 208$	$0.6 \times 0.6 \times 0.6$	9984	6 min 10 s	8

sequence) with iPAT 4 (4x1 and 24 reference lines). Furthermore, the 3D SPARKLING strategy was compared to other 3D trajectories used in Compressed Sensing MRI. First, the 3D Poisson-disk strategy introduced by Lustig et al [6] was considered. This method, which will be referred to as *Poisson-disk*, consists in acquiring along the partition direction cross-sections of 2D Poisson-disk samples with a deterministic sampling of the k-space center (see Fig. 4**c**). We used the SPARKLING algorithm to generate this sampling, by disabling the constraints on speed and acceleration. The size of the deterministically sampled region and the radially decaying rate of the density outside this region were selected using a grid-search on retrospectively subsampled reconstructions of a brain phantom image, yielding a density with decay rate of $d = 3$ and a plateau threshold of $\tau = 1$. Second, 3D radial trajectories were also acquired for comparison [5] (see Fig. 4**b**).

(a) SPARKLING **(b)** 3D radial **(c)** Poisson-disk

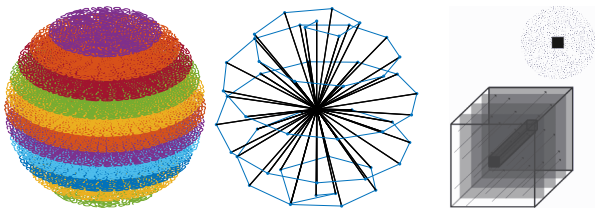

Fig. 4. 3D sampling trajectories used for the ex vivo experiments: the proposed 3D-variable-density stack-of-SPARKLING **(a)**, the 3D radial trajectories **(b)** [5] and the Poisson-disk approach **(c)** proposed in [1], [6].

For in vivo acquisitions, a stack-of-SPARKLING and a stack-of-spirals were acquired for an isotropic resolution of 0.6 mm. The SPARKLING trajectory was chosen regular in the z-direction (as in Fig. 1**a**) to allow a fair comparison with a stack-of-spirals [31] using the same imaging parameters, while a 2D variable density was used in the perpendicular plane. Because of potential sources of physiological artifacts (e.g.: off-resonance, motion) and the lower SNR of in vivo experiments, the preliminary in vivo results presented in this paper were not as much accelerated as the ex vivo experiments (see Table I).

Finally, a high resolution of 0.3 mm in the axial plane with a slice thickness of 1.5 mm was performed, similar to the protocols presented in the literature [23], [25], [32]. Here, the Cartesian reference was an iPAT 2 (24 references lines) with Partial Fourier 6/8 (phase and encode).

IV. 3D MR IMAGE RECONSTRUCTION

Images were reconstructed using a 3D extension of a self-calibrating reconstruction algorithm [33] that handles non-Cartesian k-space data collected over a multi-channel phased array and that promotes sparsity in the wavelet transform domain. The original code was implemented in Matlab and already used in [16] but an open source code is now available in Python in the PySAP software[2] both for 2D and 3D imaging. To speed up the reconstruction process in 3D imaging, the NFFT [34] was replaced with the GPU NUFFT[3]. Also, for the sake of efficiency, all 3D MR images were reconstructed using a Symmlet 8 orthogonal wavelet transform, an ℓ_1-sparsity promoting regularization. A FISTA algorithm was used to minimize the overall convex but nonsmooth objective function. For each dataset individually, the regularization parameter was grid searched over the range $(10^{-7}, 10^{-2})$ to optimize the structural similarity (SSIM) as a measure of image quality [36]. [4] Yet, the reconstruction time remained quite long, especially for treating 32 channel-receiver coil data, reaching about 4 hours for $N = 256$ and 400 iterations, including the calculation of the Lipschitz constant, with a NVIDIA GPU card GM204GL Quadro M4000 (1664 cores, global memory 8 GB). No corrections for imaging imperfections were implemented in the following results.

V. RESULTS

A. Comparison of the different SPARKLING strategies

First, different 3D SPARKLING strategies were compared for an isotropic resolution of 0.6 mm. Regular SoSPARKLING, 3D-VD SoSPARKLING and fully 3D SPARKLING trajectories were acquired for two different acquisition times: 2 min 40 s and 1 min 22 s (see Table I for details on acquisition parameters). A Cartesian iPAT 4 scan (TA = 14 min 31 s) was also collected and will be considered as the reference image quality. Results

[2]https://github.com/CEA-COSMIC/pysap
[3]https://github.com/andyschwarzl/gpuNUFFT
[4]The SSIM gives an image quality score relatively to a reference image. Its value lies between 0 and 1, the latter conveying a perfect match with the reference.

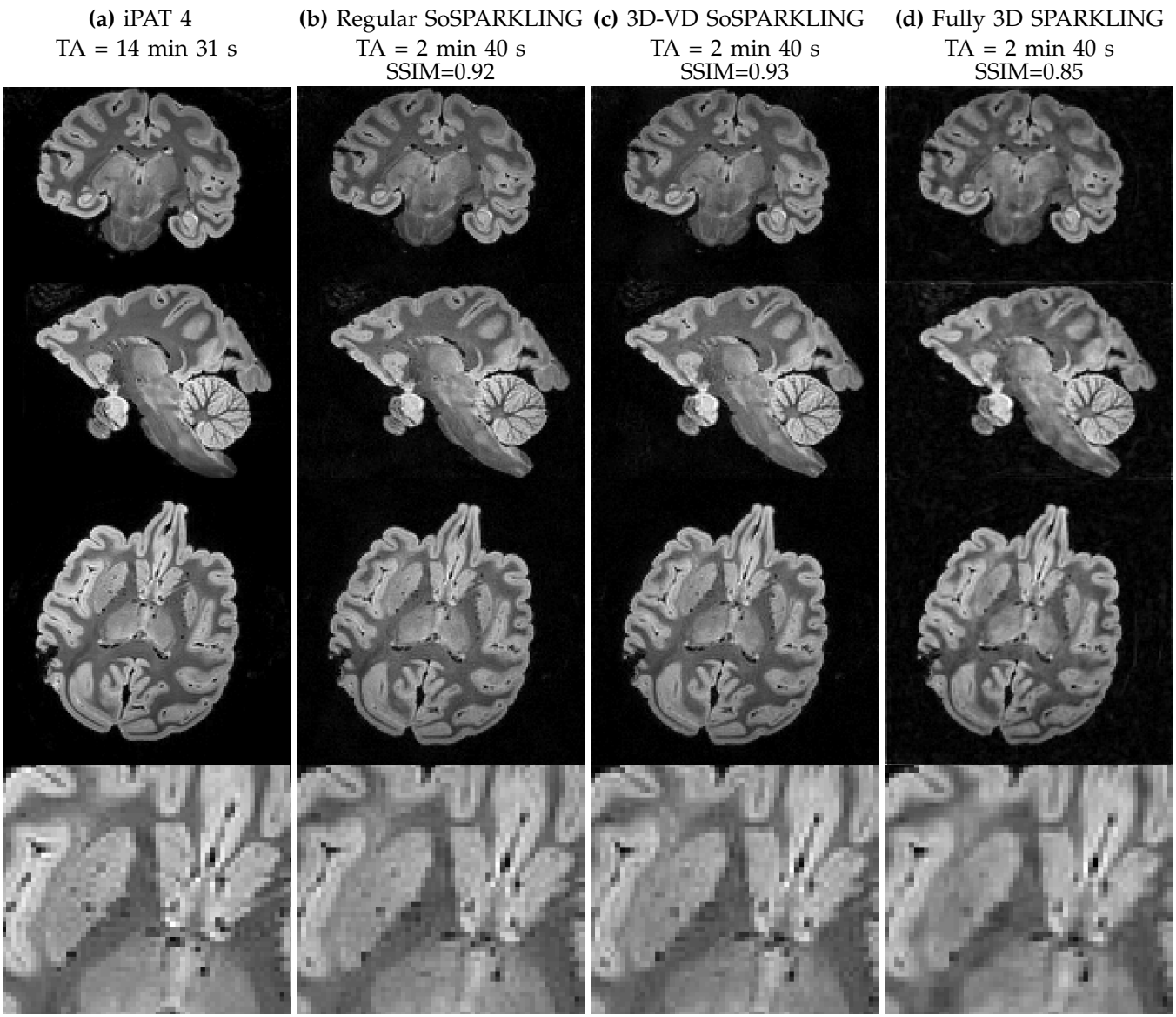

Fig. 5. 600 μm isotropic ex vivo results comparing different SPARKLING strategies. Column (a): iPAT 4 (GRAPPA) acquisition lasting TA = 14 min 31 s. Column (b): regular stack-of-SPARKLING (SoSPARKLING) results for an acquisition time of TA = 2 min 40 s. Column (c): 3D-variable-density SoSPARKLING for an acquisition time of TA=2 min 40 s. Column (d): fully 3D SPARKLING for an acquisition time of TA = 2 min 40s. Rows 1 to 4 respectively display coronal slices, sagittal slices, axial slices and a magnified region of the latter axial slices. FOV was $200 \times 200 \times 140$ mm^3.

in transversal, coronal, sagittal planes and a magnified central region of the axial slice are shown in Fig. 5 for a SPARKLING acquisition time of 2 min 40 s. Each column corresponds to a different sampling method. For both scan times (see Supplementary Material Fig. 1 for 1 min 22 s results), the image quality is well preserved especially the dendritic arborization in the cerebellum, which is visible in the sagittal plane. One may notice that the fully 3D SPARKLING results appear slightly blurrier than the SoSPARKLING results. Regular and 3D-VD SoSPARKLING yield similar image quality as is corroborated by the 3D SSIM scores measured with the iPAT 4 image as a reference.

B. Comparison with existing sampling trajectories

1) Ex vivo results: 3D SPARKLING trajectories were also compared to 3D radial and Poisson-disk sampling strategies for an isotropic resolution of 0.6 mm and a very short acquisition time of 45 s, corresponding to a number of 1140 shots. Here, a 3D-variable-density stack-of-SPARKLING was used for SPARKLING acquisitions since it yielded better image quality among the previously tested 3D SPARKLING strategies and has the advantage of supporting high acceleration factors while densely covering the low frequencies. Indeed, at this acceleration factor, a regular SoSPARKLING would only have 5 shots per plane while the 3D-VD SoSPARKLING presents twice as many shots in the center of the k-space. Moreover, a standard GRAPPA-accelerated Carte-

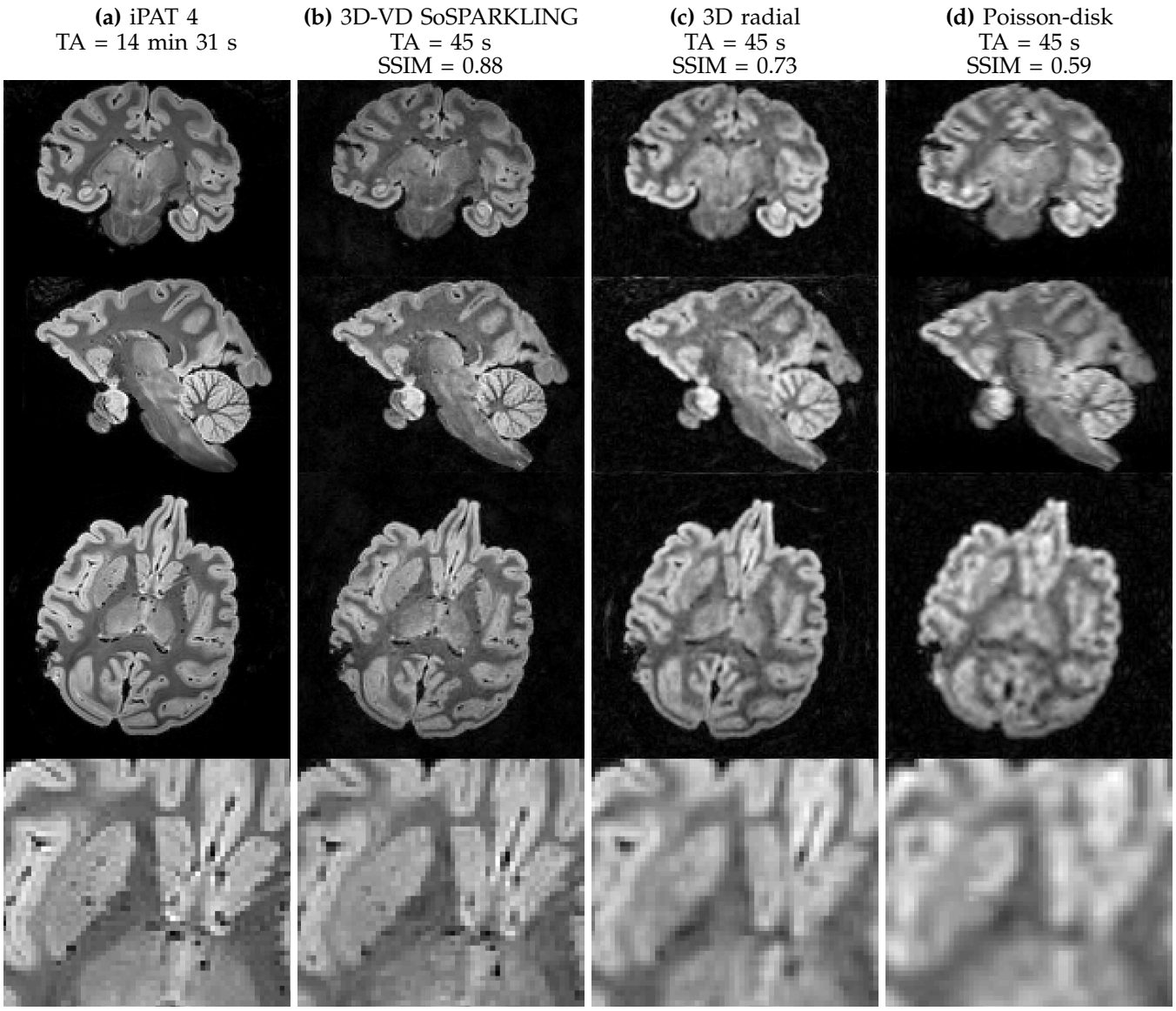

Fig. 6. Ex vivo results of 0.6 mm isotropic resolution comparing 3D-variable density stack-of-sparkling (3D-VD SoSPARKLING) **(b)**, 3D radial **(c)** and 3D Poisson-disk lines **(d)** samplings for a total number of shots of 1140, i.e., an acquisition time of 45 s. Reference scan in **(a)** is an iPAT 4 (GRAPPA) acquisition lasting TA = 14 min 31 s. Rows 1 to 4 respectively display coronal slices, sagittal slices, axial slices and a magnified region of the latter axial slices. FOV was $200 \times 200 \times 140$ mm^3.

sian scans was also performed for an iPAT of 4 lasting 14 min 31 s. Results are shown in Fig. 6 for coronal, sagittal, axial planes and a magnified central region of the axial image. Each column corresponds to a different acquisition strategy.

Of all 45-second scans, the SPARKLING method presents the best image quality. The dendritic arborization in the cerebellum in the sagittal slice and the magnified region of the axial slice both appear significantly blurrier in the 3D radial and the Poisson-disk strategies compared to the SPARKLING acquisition. These visual observations are corroborated by the SSIM scores: the SSIM of the SPARKLING image is increased by 20% compared to the 3D radial trajectories and by 50% for the Poisson-disk trajectories.

C. In vivo results

Fig. 7 shows preliminary results of an in vivo scan with 0.6 mm isotropic resolution acquired with a stack-of-SPARKLING at 7 Tesla. The stack-of-SPARKLING was composed of 208 identical 2D trajectroies of 48 shots each, corresponding to a scan time of 6 min 10 s. Compared to the Cartesian scan (first column) which is 2.5 times as long, both non-Cartesian acquisitions suffer from off-resonance effects, but the stack-of-spirals acquisition (third column) is significantly more affected than the SPARKLING scan (second column). In particular, the axial slices of the spiral image reveal severe distortions in the orbitofrontal cortex. Moreover, the spiral acquisition presents a reduced effective resolution compared to the SPARKLING scan whose resolution remains close to the Cartesian one. This is visible in the coronal slices

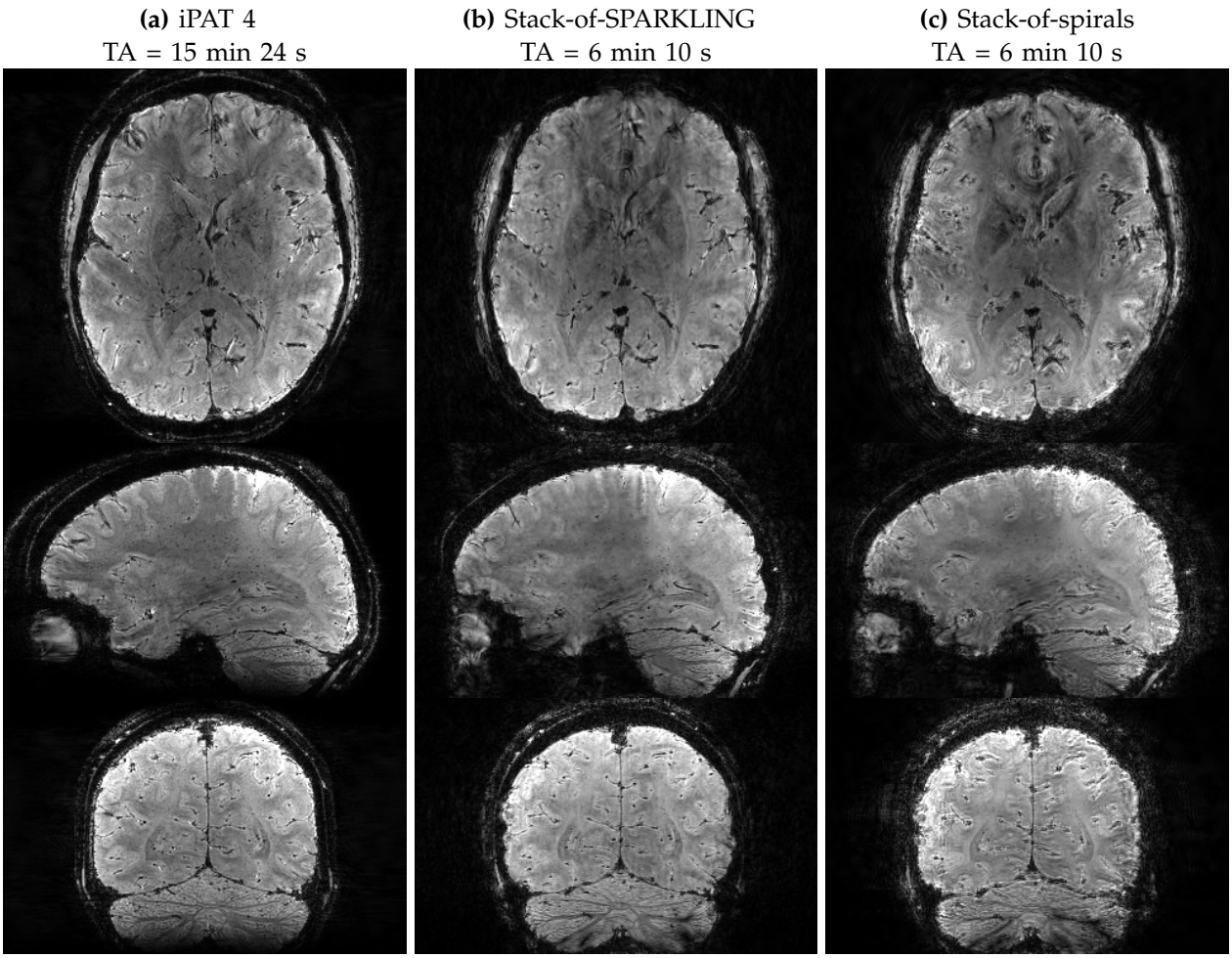

Fig. 7. In vivo results of 0.6 mm isotropic resolution comparing regular stack-of-SPARKLING (SoSPARKLING) **(b)** and a stack-of-spirals **(c)** samplings (with a 2D variable density in each plane) for a total of 9984 shots, i.e., an acquisition time of 6 min 10 s. Rows 1 to 3 respectively display axial, sagittal and coronal slices. The spiral images present more severe off-resonance artifacts compared to the SPARLKING scan (see orbitofrontal region in axial slices). Reference scan in **(a)** is an iPAT 4 (GRAPPA) acquisition lasting TA = 15 min 24 s. FOV was $230 \times 230 \times 124$ mm^3.

showing a cerebellum which is better defined in the SPARKLING image.

D. High in plane resolution

Finally, images were acquired at a high in plane resolution of 0.3 mm with a slice thickness of 1.5 mm. A standard iPAT 2 PF 6/8 (phase and slice) scan was collected, which is commonly used in the literature of GRE for susceptibility weighted imaging (SWI) at 7 Tesla [23], and is shown in Fig. 8**a**. SPARKLING-accelerated acquisitions were also performed for an acquisition time of 2 min 43 s and 1 min 24 s as illustrated in Fig. 8**b-c**. Given the small number of slices in this application, we used a regular stack-of-SPARKLING for this acquisition. We can observe that the SPARKLING acquisitions yield good image quality although 4 and 10 times faster than the Cartesian scan, respectively.[5]

[5]The iPAT image in Fig. 8**a** which was reconstructed with the online scanner reconstructor presented a sub-pixel offset compared to the center of the image and the SPARKLING reconstructions, which is why SSIM scores were not calculated in this case.

VI. Discussion

Among the three studied approaches of 3D SPARKLING (i.e., regular stack-of-SPARKLING, 3D-variable-density stack-of-SPARKLING and fully 3D SPARKLING), we observed that the 3D-variable-density stack-of-SPARKLING was performing best. The latter strategy performs a 3D variable density, thus allowing to trade high spatial frequencies for lower frequency content, in contrast to the regular SoSPARKLING. It thus pushes the undersampling factor even further.

Regarding the performance of the fully 3D SPARKLING which was slightly behind the SoSPARKLING strategies, one may propose several explanations. First, the constraint to generate the shots *separately* introduced some structure in the sampling, which leads to a degraded global distribution of the samples compared to 2D SPARKLING. To investigate this in more detail, it can be useful to look at all the samples of a 3D SPARKLING trajectory present in a plane of thickness one k-space pixel. These plane sections are shown in Fig. 9 for different axes

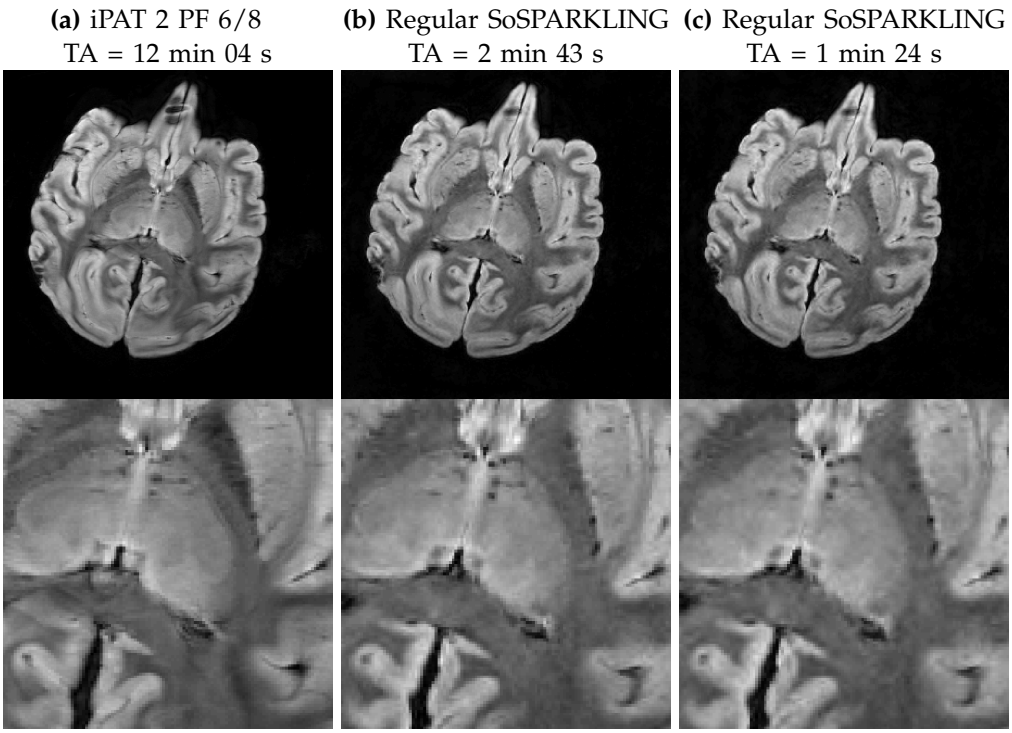

Fig. 8. Ex vivo results of high in plane resolution of 0.3 mm and 1.5-mm slice thickness for 96 slices. **(a)**, the reference Cartesian scan used iPAT 2 with partial Fourier 6/8 (phase and slice encode) and lasted 12 min 04 s. The two regular stacks-of-sparkling (SoSPARKLING) schemes were composed of 2090 shots **(b)** and 4085 shots **(c)**, corresponding to acquisition times of 1 min 24 s and 2 min 43 s, respectively. FOV was $200 \times 200 \times 140$ mm^3.

and altitudes. Overall, asymmetric structures can be observed in these plane sections, due to the rotation of one SPARKLING shot to fill one k-space latitude. In addition, the distribution of the samples is not as well controlled as it was for 2D SPARKLING, in terms of local uniformity for instance. Moreover, the center of the k-space seems to be critical as well: since the samples of different shots are not interacting, the global distribution of the samples in the center is not perfect, with possible under- or over-sampling. Hence, the fully 3D SPARKLING approach may be significantly improved by generating all the shots at once. This would however require a considerable development to maintain a reasonable computational time.

In this work, we used the accelerated 3D SPARKLING trajectories to acquire T_2^*-weighted images of an ex vivo baboon brain at a high isotropic resolution of 0.6 mm for a FOV of $200 \times 200 \times 140$ mm^3. If the iPAT 4 acquisition is considered as a reference scan, the proposed method allowed to divide the acquisition time by a factor of 20, reducing the scan time from 14 min 31 s to 45 s, while maintaining good image quality. For the studied imaging protocol, we also compared the SPARKLING method to other 3D methods such as 3D radial and the Poisson-disk proposed by Lustig et al., for the same acquisition time of 45 s. The proposed method performed significantly better than the latter two techniques which both appeared blurry, confirming the inefficiency of sampling along straight lines in the considered context. In this regard, the corkscrew pattern proposed in the recent

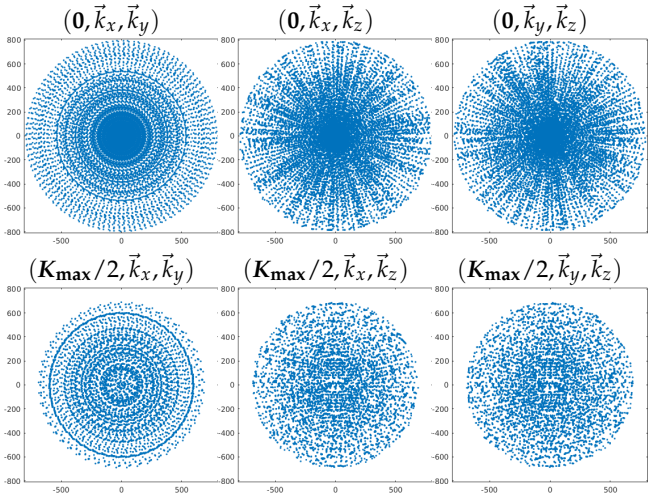

Fig. 9. From left to right: plane sections of an isotropic fully 3D SPARKLING trajectory showing all the samples contained in a plane of thickness one k-space pixel ($1/FOV$). The plane sections are crossing the origin $\mathbf{0} = (0,0,0)$ (top row) of the k-space or half the maximum spatial frequency $\boldsymbol{K}_{\mathbf{max}}/2 = (\frac{K_{\max}}{2}, \frac{K_{\max}}{2}, \frac{K_{\max}}{2})$ (bottom row) for different directions. Because of isotropy, we used the same $K_{\max}$ over all axes.

wave-CAIPI strategy [37] may improve the sampling efficiency although it was not originally proposed for variable density sampling in the context of Compressed Sensing. Furthermore, for a high in plane resolution of 0.3 mm, a slice thickness of 1.5 mm and a FOV of $200 \times 200 \times 140$ mm^3, the SPARKLING method was also able to significantly reduce the acquisition time.

Compared to the standard sequence used in the context of high resolution SWI (iPAT 2 Partial Fourier 6/8) which lasted 12 min 04 s, the proposed method yielded a similar image quality in only 1 min 24 s. Perhaps, the acceleration could be pushed even further and enable to reduce the acquisition time below one minute while still presenting diagnostic image quality.

Finally, we also showed results of in vivo acquisitions with a stack-of-SPARKLING for a 0.6 mm isotropic resolution and an acquisition time of 6 minutes. Consistent with the findings of [16], the SPARKLING method showed a reduced sensitivity to artifacts that are typical of long readouts (e.g. off-resonance and encoding errors) compared to the stack-of-spirals. Although these preliminary results are encouraging, they are yet to be fully validated with further in vivo acquisitions exploring a broader range of acceleration factors and adding acceleration in the partition direction as well.

All in all, as long as the readout duration and the gradient constraints allow the SPARKLING trajectories to deviate from the initial input pattern, our method should lead to better image quality than predetermined parameterized families such as spirals or lines since all the versatility of the gradients is exploited. However, let us emphasize that the longer the readouts, the more we should expect from SPARKLING, since more circumvolutions are allowed. The T_2^* contrast was therefore a natural application for the SPARKLING method.

VII. Conclusions

In this work, we proposed to use a variable-density SPARKLING strategy to accelerate the scan time of high resolution T_2^*-weighted 3D acquisitions. Among the three studied approaches of 3D SPARKLING, the stack-of-SPARKLING with a 3D variable density and a number of shots varying along the partition direction was observed to perform best. Compared to a reference iPAT4 Cartesian scan, the proposed method allowed to divide the scan time of ex vivo acquisitions by a factor of 20, while maintaining good image quality at a 0.6 mm isotropic resolution. In the presented ex vivo experiments, the proposed method performed significantly better than 3D radial and the Poisson-disk which both appeared blurry for the same acquisition time of 45 s. The 3D SPARKLING method was also used for a very high in plane resolution of 0.3 mm and was shown to maintain a good image quality in just 2 minutes compared to the reference Cartesian scan of 12 minutes. Finally, preliminary in vivo results showed that a stack-of-SPARKLING is less sensitive to artifacts compared to a stack-of-spirals. A straightforward application may be ultrafast 3D susceptibility-weighted imaging [23].

Acknowledgements

This research program was supported by a 2016 DRF Impulsion grant (COSMIC, P.I.: P.C.). C.L. was also supported by the CEA international PhD program. P.W. was supported by the ANR JCJC OMS. We would like to thank Nicolas Boulant for his insightful remarks. The authors are thankful to Dr Patrick Martigne (Department of Radiobiology, IRBA, Brétigny-sur-Orge, France) for the preparation of the ex vivo baboon brain. This work was supported by the Leducq Foundation (large equipment ERPT program, NEUROVASC7T project).

References

[1] M. Lustig, D. Donoho, and J. M. Pauly, "Sparse MRI: The application of compressed sensing for rapid MR imaging," *Magnetic Resonance in Medicine*, vol. 58, no. 6, pp. 1182–1195, 2007.

[2] G. Puy, P. Vandergheynst, and Y. Wiaux, "On variable density compressive sampling," *IEEE Signal Processing Letters*, vol. 18, no. 10, pp. 595–598, 2011.

[3] B. Adcock, A. C. Hansen, C. Poon, and B. Roman, "Breaking the coherence barrier: A new theory for compressed sensing," vol. 5, 2017.

[4] C. Boyer, J. Bigot, and P. Weiss, "Compressed sensing with structured sparsity and structured acquisition," *Applied and Computational Harmonic Analysis*, 2017.

[5] P. E. Larson, P. T. Gurney, and D. G. Nishimura, "Anisotropic field-of-views in radial imaging," *IEEE Transactions on Medical Imaging*, vol. 27, no. 1, pp. 47–57, 2008.

[6] S. S. Vasanawala, M. T. Alley, B. A. Hargreaves, R. A. Barth, J. M. Pauly, and M. Lustig, "Improved pediatric MR imaging with compressed sensing," *Radiology*, vol. 256, no. 2, pp. 607–616, 2010.

[7] P. Irarrazabal and D. G. Nishimura, "Fast three dimensional magnetic resonance imaging," *Magnetic Resonance in Medicine*, vol. 33, no. 5, pp. 656–662, 1995.

[8] F. E. Boada, J. S. Gillen, G. X. Shen, S. Y. Chang, and K. R. Thulborn, "Fast three dimensional sodium imaging," *Magnetic Resonance in Medicine*, vol. 37, no. 5, pp. 706–715, 1997.

[9] G. Valvano, N. Martini, L. Landini, and M. F. Santarelli, "Variable density randomized stack of spirals(VDR-SoS) for compressive sensing MRI," *Magnetic Resonance in Medicine*, vol. 76, no. 1, pp. 59–69, 2016.

[10] K. M. Johnson, "Hybrid radial-cones trajectory for accelerated MRI," *Magnetic Resonance in Medicine*, vol. 77, no. 3, pp. 1068–1081, 2017.

[11] B. M. Dale, J. S. Lewin, and J. L. Duerk, "Optimal design of *k*-space trajectories using a multi-objective genetic algorithm," *Magnetic Resonance in Medicine*, vol. 52, no. 4, pp. 831–841, 2004.

[12] R. Mir, A. Guesalaga, J. Spiniak, M. Guarini, and P. Irarrazaval, "Fast three-dimensional *k*-space trajectory design using missile guidance ideas," *Magnetic Resonance in Medicine*, vol. 52, no. 2, pp. 329–336, 2004.

[13] C. Kumar Anand, A. Thomas Curtis, and R. Kumar, "Durga: A heuristically-optimized data collection strategy for volumetric magnetic resonance imaging," *Engineering Optimization*, vol. 40, no. 2, pp. 117–136, 2008.

[14] N. Chauffert, P. Ciuciu, J. Kahn, and P. Weiss, "A projection method on measures sets," *Constructive Approximation*, vol. 45, no. 1, pp. 83–111, 2017.

[15] C. Boyer, N. Chauffert, P. Ciuciu, J. Kahn, and P. Weiss, "On the generation of sampling schemes for magnetic resonance imaging," *SIAM Journal on Imaging Sciences*, vol. 9, no. 4, pp. 2039–2072, 2016.

[16] C. Lazarus, P. Weiss, N. Chauffert, F. Mauconduit, L. El Gueddari, C. Destrieux, I. Zemmoura, A. Vignaud, and P. Ciuciu, "SPARKLING: variable-density k-space filling curves for accelerated T2*-weighted MRI," *Magnetic Resonance in Medicine*, Jan. 2019.

[17] H. K. Song and L. Dougherty, "Dynamic MRI with projection reconstruction and KWIC processing for simultaneous high spatial and temporal resolution," *Magnetic Resonance in Medicine*, vol. 52, no. 4, pp. 815–824, 2004.

[18] W. Lin, J. Guo, M. A. Rosen, and H. K. Song, "Respiratory motion-compensated radial dynamic contrast-enhanced (DCE)-MRI of chest and abdominal lesions," *Magnetic Resonance in Medicine*, vol. 60, no. 5, pp. 1135–1146, 2008.

[19] D. R. Thedens, P. Irarrazaval, T. S. Sachs, C. H. Meyer, and D. G. Nishimura, "Fast magnetic resonance coronary angiography with a three-dimensional stack of spirals trajectory," *Magnetic Resonance in Medicine*, vol. 41, no. 6, pp. 1170–1179, 1999.

[20] P. Börnert and D. Jensen, "Coronary artery imaging at 0.5 T using segmented 3D echo planar imaging," *Magnetic Resonance in Medicine*, vol. 34, no. 6, pp. 779–785, 1995.

[21] L. Kasper, M. Engel, C. Barmet, J. Reber, J. Heinzle, K. E. Stephan, and P. K. Paul, "Rapid 3D blipped spiral fMRI at 7 T," in *Proc. Intl. Soc. Mag. Reson. Med.*, vol. 26, no. 5461, 2018.

[22] D. Stäb, S. Bollmann, C. Langkammer, K. Bredies, and M. Barth, "Accelerated mapping of magnetic susceptibility using 3D planes-on-a-paddlewheel (POP) EPI at ultra-high field strength," *NMR in Biomedicine*, vol. 30, no. 4, p. e3620, 2017.

[23] A. Abosch, E. Yacoub, K. Ugurbil, and N. Harel, "An assessment of current brain targets for deep brain stimulation surgery with susceptibility-weighted imaging at 7 Tesla," *Neurosurgery*, vol. 67, no. 6, pp. 1745–1756, 2010.

[24] C. Lenglet, A. Abosch, E. Yacoub, F. De Martino, G. Sapiro, and N. Harel, "Comprehensive in vivo mapping of the human basal ganglia and thalamic connectome in individuals using 7T MRI," *PloS One*, vol. 7, no. 1, p. e29153, 2012.

[25] C. Moenninghoff, O. Kraff, S. Maderwald, L. Umutlu, J. M. Theysohn, A. Ringelstein, K. H. Wrede, C. Deuschl, J. Altmeppen, M. E. Ladd *et al.*, "Diffuse axonal injury at ultra-high field MRI," *PLoS One*, vol. 10, no. 3, p. e0122329, 2015.

[26] N. Chauffert, P. Weiss, J. Kahn, and P. Ciuciu, "A projection algorithm for gradient waveforms design in Magnetic Resonance Imaging," *IEEE Transactions on Medical Imaging*, vol. 35, no. 9, pp. 2026–2039, Sep. 2016.

[27] C. Schmaltz, P. Gwosdek, A. Bruhn, and J. Weickert, "Electrostatic halftoning," in *Computer Graphics Forum*, vol. 29, no. 8. Wiley Online Library, 2010, pp. 2313–2327.

[28] T. Teuber, G. Steidl, P. Gwosdek, C. Schmaltz, and J. Weickert, "Dithering by differences of convex functions," *SIAM Journal on Imaging Sciences*, vol. 4, no. 1, pp. 79–108, 2011.

[29] P. Leopardi, "A partition of the unit sphere into regions of equal area and small diameter," *Electronic Transactions on Numerical Analysis*, vol. 25, no. 12, pp. 309–327, 2006.

[30] S. Lloyd, "Least squares quantization in PCM," *IEEE Transactions on Information Theory*, vol. 28, no. 2, pp. 129–137, 1982.

[31] J. H. Lee, B. A. Hargreaves, B. S. Hu, and D. G. Nishimura, "Fast 3D imaging using variable-density spiral trajectories with applications to limb perfusion," *Magnetic Resonance in Medicine*, vol. 50, no. 6, pp. 1276–1285, 2003.

[32] M. A. Schmidt, T. Engelhorn, F. Marxreiter, J. Winkler, S. Lang, S. Kloska, P. Goelitz, and A. Doerfler, "Ultra high-field SWI of the substantia nigra at 7T: reliability and consistency of the swallow-tail sign," *BMC neurology*, vol. 17, no. 1, p. 194, 2017.

[33] L. El Gueddari, C. Lazarus, H. Carrié, A. Vignaud, and P. Ciuciu, "Self-calibrating nonlinear reconstruction algorithms for variable density sampling and parallel reception MRI," in *10th IEEE Sensory Array and Multichannel (SAM) signal processing workshop*, Sheffield, UK, Jul. 2018, pp. 415–419.

[34] J. Keiner, S. Kunis, and D. Potts, "Using NFFT 3—A Software Library for Various Nonequispaced Fast Fourier Transforms," *ACM Transactions on Mathematical Software (TOMS)*, vol. 36, no. 4, p. 19, 2009.

[35] J.-M. Lin, "Python Non-Uniform Fast Fourier Transform (PyNUFFT): An Accelerated Non-Cartesian MRI Package on a Heterogeneous Platform (CPU/GPU)," *Journal of Imaging*, vol. 4, no. 3, p. 51, 2018.

[36] Z. Wang, A. C. Bovik, H. R. Sheikh, and E. P. Simoncelli, "Image quality assessment: from error visibility to structural similarity," *IEEE Transactions on Image Processing*, vol. 13, no. 4, pp. 600–612, 2004.

[37] B. Bilgic, B. A. Gagoski, S. F. Cauley, A. P. Fan, J. R. Polimeni, P. E. Grant, L. L. Wald, and K. Setsompop, "Wave-CAIPI for highly accelerated 3D imaging," *Magnetic Resonance in Medicine*, vol. 73, no. 6, pp. 2152–2162, 2015.

[38] B. E. Dietrich, D. O. Brunner, B. J. Wilm, C. Barmet, S. Gross, L. Kasper, M. Haeberlin, T. Schmid, S. J. Vannesjo, and K. P. Pruessmann, "A field camera for MR sequence monitoring and system analysis," *Magnetic Resonance in Medicine*, vol. 75, no. 4, pp. 1831–1840, 2016.

[39] S. J. Vannesjo, N. N. Graedel, L. Kasper, S. Gross, J. Busch, M. Haeberlin, C. Barmet, and K. P. Pruessmann, "Image reconstruction using a gradient impulse response model for trajectory prediction," *Magnetic Resonance in Medicine*, vol. 76, no. 1, pp. 45–58, 2016.